WAVE DISPERSION STUDY IN THE INDIAN OCEAN TSUNAMI OF DECEMBER 26, 2004

Juan Horrillo and Zygmunt Kowalik
Institute of Marine Science
University of Alaska Fairbanks
Fairbanks, Alaska

Yoshinori Shigihara
National Defense Academy of Japan.

ABSTRACT

A numerical study which takes into account wave dispersion effects has been carried out in the Indian Ocean to reproduce the initial stage of wave propagation of the tsunami event occurred on December 26, 2004. Three different numerical models have been used: the nonlinear shallow water (nondispersive), the nonlinear Boussinesq and the full Navier-Stokes aided by the volume of fluid method to track the free surface. Numerical model results are compared against each other. General features of the wave propagation agreed very well in all numerical studies. However some important differences are observed in the wave patterns, i.e., the development in time of the wave front is shown to be strongly connected to the dispersion effects. Discussions and conclusions are made about the spatial and temporal distribution of the free surface reaffirming that the dispersion mechanism is important for tsunami hazard mitigation.

INTRODUCTION

The recorded and observed tsunami waves originated by earthquake of 26 December, 2004 showed complicated temporal and spatial structure, since the initial wave generated by the bottom uplift had multiple amplitude and frequency components.

Analysis of the recorded data demonstrated that the tsunami waves propagating southwestward across the Indian Ocean two hours after the main shock were noticeably dispersive (Kulikov, 2005). Dispersion effects can be significant for amplitude estimation in transoceanic tsunami propagation. This brings into question the accuracy of the model used for numerical simulations of tsunamis. Usually, tsunami models are based on the shallow water approximation which ignores the effect of linear wave dispersion.

As the initial wave propagates, separation of the wave into spectral components with different frequencies and amplitudes occurs. Thus, the leading wave is followed by a train of waves formed in its tail. In coastal regions this train of waves interacts with the leading wave's runup, drawdown and reflection from shelf or land, introducing strong modification to leading wave effects. We aim, therefore, to infer the role of the dispersion effects in tsunami wave modification.

Often populated areas along coasts are located in low-lying and flat regions that together with natural and man made obstacles make the retreat of the flood caused by the first tsunami wave very slow. Under this situation, subsequent waves as they shallow often ride over a region already flooded by the first wave allowing these waves to impinge on structures, often with higher sea level and speed.

The multiple wave phenomenon was observed throughout the Sri Lanka coast, as described in John Headland's report at the ASCE web page (http://www.asce.org/page/?id=53.). The first few rows of houses were destroyed by the tsunami wave, and acted to dissipate it. Interior houses, as a result, were not as extensively damaged. In another location along the coast; one witness said. 'It wasn't one wave, it came in great surges, each one deeper than the last and pushing the water that had come in before in front of it'. In fact, most witnesses talked of three main waves. The first knocked them off their feet, the second picked them up and carried them, often at up to 50 km/h, and the third, the most powerful, bore them high, up to 15 m in some places or sucked them under. To explain these phenomena is not a simple task, since a train of waves approaching a particular coastal region, in addition to the transformation it may have experienced by dispersion effects, could be composed of a combination of waves coming from different parts of the source or it may be that these waves have been diverted by the ocean bathymetry or transformed by a submerged bar. Since this study intends to investigate the role of dispersion effects in tsunami calculations and its possible implication in propagation and runup, simplified model setups are used (one/two-dimensional) so that tsunami physics and behavior can be better explained.

Several studies have highlighted the importance of dispersion effect in tsunami propagation. Sato (1996), in the numerical calculation of the 1993 Okushiri Island tsunami, found that local tsunami enhancement can be explained by a series of dispersive waves which ride on the main tsunami front. Ortiz *et al.* (2001) suggested that the frequency dispersion mechanism, as prescribed by dispersive theory plays the main role in propagation of large and medium-size tsunamis. Heinrich *et al.* (1998) using the Boussinesq approach, found that the effect of dispersion can be significant. Imamura *et*

al. (1988, 1990) and Liu *et al.* (1995) also considered the effect to be important.

In tsunami calculations the dispersive effects are usually considered through the Boussinesq equation, Dunbar *et al.* (1991); Madsen *et al.* (1999). Their numerical solutions require small space steps and often implicit schemes are used due to stringent numerical stability requirement (Shigihara, 2004). As the second order approximation to the numerical schemes leads to an error of approximation proportional to the third derivative, and since the dispersion terms in the Boussinesq equation also depend on the third derivative, Imamura and Shuto (1989) constructed a numerical scheme which uses numerical dispersion to simulate physical dispersion. This scheme was improved and applied to the propagation of tsunamis over slowly varying topography by Yoon (2002), thus opening the possibility to account for the dispersion of distant tsunamis. In the runup region, at the steep wave front where the tsunami wave starts to break, the dispersive effects due to physical processes tend to interact with the short wave numerical instability generating turbulent motion. To suppress such oscillations, Goto and Shuto (1983) and Sato (1996) suggested introduction of the eddy diffusivity term. The nonlinear shallow water (NLSW, nondispersive), the nonlinear Boussinesq (NLB) and the full Navier-Stokes equations aided by the volume of fluid method to track the water surface (FNS-VOF) are important tools for the tsunami investigations. Using these tools and hydraulic experiments Fujima (2001) examined the wave transformation on large bottom obstacles. He pointed out that NLB approach when compared with experiments and FNS-VOF approach, reproduces the wave dispersion effects well.

This study aims to reproduce the Indian Ocean Tsunami (IOT) of Dec. 26, 2004 in its initial stage (two hours of tsunami wave propagation). With the help of three different numerical tools for tsunami calculation we intend to uncover some of the implications of dispersion effects in tsunami propagation and runup. The study is organized as follows: first, a brief description of the models formulation and their numerical schemes is presented. Afterwards, several numerical experiments are described based on initial conditions for free surface deformations. Then, model results are compared against each other. Finally, observations and model results are analyzed to draw conclusion on the spatial and temporal distributions of the free surface.

NUMERICAL METHODS

For the numerical computation three case studies have been carried out a) one-dimension: the channel case; b) two-dimension: the Bay of Bengal case; c) one-dimension Yala/Banda-Aceh cases. In case a) an imaginary channel along a given transect is chosen. A study is made for validation and comparison of the models (NLB and FNS-VOF) to show dispersive properties of tsunami and limitations of the NLSW approach. In case b) a small domain which encompasses the south part of the Bay of Bengal is used for the numerical simulations. Comparisons are made between NLB and NLSW models to uncover dispersive effects. In case c) simplified studies in which one-dimensional channels are used again to reveal wave runup of dispersive waves. The NLSW and NLB models are used in these cases, and initial conditions at the open side of the channels are taken from the two-dimensional models results.

In all numerical simulation, the bathymetry is taken From GEBCO data bank using 1 min resolution. The bathymetric profile along transects (one-dimensional cases) are obtained by linear interpolation from the GEBCO data bank. Initial condition for the free

surface deformation is detailed in Kowalik *et al.* (2005) according to the static dislocation formulae from Okada (1985).

Description of NLSW Model

The nonlinear shallow water equations of motion and continuity are taken in the following form (Kowalik and Murty 1993a)

$$\frac{\partial u}{\partial t} + u\frac{\partial u}{\partial x} + v\frac{\partial u}{\partial y} + g\frac{\partial \zeta}{\partial x} + \frac{1}{\rho D} ru\sqrt{u^2 + v^2} = 0, \tag{1}$$

$$\frac{\partial v}{\partial t} + u\frac{\partial v}{\partial x} + v\frac{\partial v}{\partial y} + g\frac{\partial \zeta}{\partial y} + \frac{1}{\rho D} rv\sqrt{u^2 + v^2} = 0, \tag{2}$$

$$\frac{\partial \zeta}{\partial t} + \frac{\partial uD}{\partial x} + \frac{\partial vD}{\partial y} = 0, \tag{3}$$

where ρ is the water density, u and v are vertically averaged velocity components along x and y directions respectively, H is the mean water depth, ζ is the sea level, $D = (\zeta + H)$ is the total depth, r is the friction coefficient, and g is the gravitational acceleration.

Above equations are solved numerically by using a staggered grid (C grid) in space as shown in Fig. 1. Velocity locations for u and v are denoted by horizontal and vertical bars respectively. The u velocity grid points are offset from the v velocity grid points. Sea level locations are denoted by crosses. Velocity components and sea level (u, v and ζ) are organized into triplets as shown by the triangles. The depth is defined at the sea level location. To resolve the nonlinear terms in the equations of motion the v velocity is needed at the u locations and vice versa. To visualize how the averaged values are constructed, dark-gray and plain-gray circles are introduced at the velocity locations. The values of velocity marked by dark-gray circles, when they are averaged, will define the average of v velocity at the u location. The average of v velocity at this location is

$$\overline{v} = 0.25(v_{j,k-1} + v_{j,k} + v_{j-1,k} + v_{j-1,k-1}).$$

In a similar way the average of u velocities (plain-gray circles) at the v point is

$$\overline{u} = 0.25(u_{j+1,k} + u_{j+1,k+1} + u_{j,k+1} + u_{j,k}).$$

The grid size (space step) along the E-W direction is h_x, and the distance is jh_x, index $j = 1,\ldots$. The space step along the N-S direction is h_y and the distance is kh_y, index $k = 1,\ldots$.

The solution of Eqs. (1-3) is usually advanced in time by the two-time-level numerical scheme (Kowalik and Murty, 1993a). For the spatial derivatives a second order approximation is constructed, thus

$$u_{j,k}^{m+1} = u_{j,k}^{m} - \frac{gT}{h_x}(\zeta_{j,k}^{m} - \zeta_{j-1,k}^{m}) - \frac{2T}{\rho(D_{j-1,k}^{m} + D_{j,k}^{m})} ru_{j,k}^{m}\sqrt{(u_{j,k}^{m})^2 + (\overline{v}^{m})^2}$$

$$- \frac{u_p^m T}{h_x}(u_{j,k}^{m} - u_{j-1,k}^{m}) - \frac{u_n^m T}{h_x}(u_{j+1,k}^{m} - u_{j,k}^{m})$$

$$-\frac{\overline{v}_p^m T}{h_y}(u_{j,k}^m - u_{j,k-1}^m) - \frac{\overline{v}_n^m T}{h_y}(u_{j,k+1}^m - u_{j,k}^m), \tag{4}$$

$$\begin{aligned} v_{j,k}^{m+1} = v_{j,k}^m &- \frac{gT}{h_y}(\zeta_{j,k+1}^m - \zeta_{j,k}^m) - \frac{2T}{\rho(D_{j,k}^m + D_{j,k+1}^m)} r v_{j,k}^m \sqrt{(\overline{u}^m)^2 + (v_{j,k}^m)^2} \\ &- \frac{\overline{u}_p^m T}{h_x}(v_{j,k}^m - v_{j-1,k}^m) - \frac{\overline{u}_n^m T}{h_x}(v_{j+1,k}^m - v_{j,k}^m) \\ &- \frac{v_p^m T}{h_y}(v_{j,k}^m - v_{j,k-1}^m) - \frac{v_n^m T}{h_y}(v_{j,k+1}^m - v_{j,k}^m), \end{aligned} \tag{5}$$

where index m stands for the time stepping, T is the time step. $u_p = 0.5(u_{j,k} + |u_{j,k}|)$, $u_n = 0.5(u_{j,k} - |u_{j,k}|)$, $v_p = 0.5(v_{j,k} + |v_{j,k}|)$ and $v_n = 0.5(v_{j,k} - |v_{j,k}|)$ are velocity switches used in the upwind/downwind method to turn on/off the upstream/downstream advective term derivatives, i.e., if $u_{j,k} > 0$ then $u_p = u_{i,j}$ and $u_n = 0$; conversely, if $u_{j,k} < 0$ then $u_p = 0$ and $u_n = u_{j,k}$.

For the large scale computations the upwind/downwind method is essential as it displays strong stability. In order to obtain a higher order approximation in space for the continuity equation the upwind/downwind numerical scheme proposed by Mader (2004) is expanded. The numerical scheme has been improved by an additional interpolation between grid points based on the method of characteristic. Then, the continuity equation becomes

$$\begin{aligned} \zeta_{j,k}^{m+1} = \zeta_{j,k}^m &- \frac{T}{h_x}(flux_{x,j+1,k} - flux_{x,j,k}) \\ &- \frac{T}{h_y}(flux_{y,j,k} - flux_{y,j,k-1}), \end{aligned} \tag{6}$$

where

$$flux_{x,j,k} = u_p^{m+1}\zeta_{p,x} + u_n^{m+1}\zeta_{n,x} + u_{j,k}^{m+1}\frac{(H_{j,k} + H_{j-1,k})}{2}, \tag{7}$$

$$\zeta_{p,x} = (0.5 + u_p^{m+1}\frac{T}{h_x})\zeta_{j-1,k}^m + (0.5 - u_p^{m+1}\frac{T}{h_x})\zeta_{j,k}^m, \tag{8}$$

$$\zeta_{n,x} = (0.5 + u_n^{m+1}\frac{T}{h_x})\zeta_{j-1,k}^m + (0.5 - u_n^{m+1}\frac{T}{h_x})\zeta_{j,k}^m, \tag{9}$$

$$flux_{y,j,k} = v_p^{m+1}\zeta_{p,y} + v_n^{m+1}\zeta_{n,y} + v_{j,k}^{m+1}\frac{(H_{j,k} + H_{j,k+1})}{2}, \tag{10}$$

$$\zeta_{p,y} = (0.5 + v_p^{m+1}\frac{T}{h_y})\zeta_{j,k}^m + (0.5 - v_p^{m+1}\frac{T}{h_y})\zeta_{j,k+1}^m \qquad (11)$$

$$\zeta_{n,y} = (0.5 + v_n^{m+1}\frac{T}{h_y})\zeta_{j,k}^m + (0.5 - v_n^{m+1}\frac{T}{h_y})\zeta_{j,k+1}^m . \qquad (12)$$

The numerical scheme given by Eqs. (7-12) is close to the second order of approximation in space.

For the runup condition the following step is taken, i.e., when the dry point $(j_{wet} - 1)$ is located to the left of the wet point j_{wet},

$$\text{If } (\zeta_{j_{wet}} > -H_{j_{wet}-1}) \text{ then } u_{j_{wet}} = u_{j_{wet}+1},$$

(Kowalik and Murty, 1993b).

Description of NLB Model

Equations of motion of the nonlinear Boussinesq model are taken from Shigihara et al. (2005),

$$\frac{\partial u}{\partial t} + u\frac{\partial u}{\partial x} + v\frac{\partial u}{\partial y} + g\frac{\partial \zeta}{\partial x} + \frac{1}{\rho D} ru\sqrt{u^2 + v^2} = \frac{\partial \psi}{\partial x}, \qquad (13)$$

$$\frac{\partial v}{\partial t} + u\frac{\partial v}{\partial x} + v\frac{\partial v}{\partial y} + g\frac{\partial \zeta}{\partial y} + \frac{1}{\rho D} rv\sqrt{u^2 + v^2} = \frac{\partial \psi}{\partial y}, \qquad (14)$$

where the potential function ψ is defined as

$$\psi = \frac{H^2}{3}(\frac{\partial^2 u}{\partial x \partial t} + \frac{\partial^2 v}{\partial y \partial t}). \qquad (15)$$

By substituting Eqs. (13) and (14) into Eq. (15) and neglecting both, nonlinear and bottom friction terms from the equations of motion, yields the Poisson equation for the solution of ψ as

$$\frac{H^2}{3}(\frac{\partial^2 \psi}{\partial x^2} + \frac{\partial^2 \psi}{\partial y^2}) - \psi = \frac{gH^2}{3}(\frac{\partial^2 \zeta}{\partial x^2} + \frac{\partial^2 \zeta}{\partial y^2}). \qquad (16)$$

Thus, the dispersive wave propagation results in an elliptical problem, where the potential function ψ plays the role of pressure corrector. Applying the same notation used in the previous numerical model, the finite difference forms of the equations of motion are

$$u_{j,k}^{m+1} = u_{j,k}^m - \frac{gT}{h_x}(\zeta_{j,k}^m - \zeta_{j-1,k}^m) - \frac{u_p^m T}{h_x}(u_{j,k}^m - u_{j-1,k}^m) - \frac{u_n^m T}{h_x}(u_{j+1,k}^m - u_{j,k}^m)$$
$$- \frac{\overline{v}_p^{u,m} T}{h_y}(u_{j,k}^m - u_{j,k-1}^m) - \frac{\overline{v}_n^{u,m} T}{h_y}(u_{j,k+1}^m - u_{j,k}^m)$$

$$-\frac{2T}{\rho(D^m_{j-1,k}+D^m_{j,k})}ru^m_{j,k}\sqrt{(u^m_{j,k})^2+(\overline{v}^m)^2}+\frac{T}{h_x}(\psi^m_{j,k}-\psi^m_{j-1,k}), \quad (17)$$

$$v^{m+1}_{j,k}=v^m_{j,k}-\frac{gT}{h_y}(\zeta^m_{j,k+1}-\zeta^m_{j,k})-\frac{\overline{u}^{v,m}_p T}{h_x}(v^m_{j,k}-v^m_{j-1,k})-\frac{\overline{u}^{v,m}_n T}{h_x}(v^m_{j+1,k}-v^m_{j,k})$$
$$-\frac{v^m_p T}{h_y}(v^m_{j,k}-v^m_{j,k-1})-\frac{v^m_n T}{h_y}(v^m_{j,k+1}-v^m_{j,k})$$
$$-\frac{2T}{\rho(D^m_{j,k}+D^m_{j,k+1})}rv^m_{j,k}\sqrt{(\overline{u}^m)^2+(v^m_{j,k})^2}+\frac{T}{h_y}(\psi^m_{j,k+1}-\psi^m_{j,k}). \quad (18)$$

Numerical form of the continuity equation (Eq. 3) is,

$$\zeta^{m+1}_{j,k}=\zeta^m_{j,k}-\frac{T}{h_x}(u^{m+1}_{j+1,k}D^{u,m}_{j+1,k}-u^{m+1}_{j,k}D^{u,m}_{j,k})-\frac{T}{h_y}(v^{m+1}_{j,k}D^{v,m}_{j,k}-v^{m+1}_{j,k-1}D^{v,m}_{j,k-1}). \quad (19)$$

The above explicit numerical scheme uses Eqs. (17-19) to compute velocity and sea level, where Eq. (15) serves to compute the potential function. This computational process is unstable since a new stability condition arises due to dispersive terms. It requires that the space step used for the numerical computation, h_x (assuming $h_x = h_y$), must be $h_x > 1.5H$ (Shigihara, 2004). As the average depth of the Global Ocean is close to 4km the above condition introduces relatively large space steps which lead to poor spatial resolution and numerical instability. To circumvent stability requirements an implicit numerical scheme to derive the potential function has been constructed (Shigihara *et al.* 2005). The numerical scheme uses Poisson equation (Eq. 16) in the following implicit numerical form:

$$[1+\frac{2}{3}H^2_{j,k}(\frac{1}{h_x^2}+\frac{1}{h_y^2})]\psi^{m+1}_{j,k}-\frac{H^2_{j,k}}{3}(\frac{1}{h_x^2}\psi^{m+1}_{j+1,k}+\frac{1}{h_x^2}\psi^{m+1}_{j-1,k}+\frac{1}{h_y^2}\psi^{m+1}_{j,k+1}+\frac{1}{h_y^2}\psi^{m+1}_{j,k-1})$$
$$=\frac{gH^2_{j,k}}{3}[2(\frac{1}{h_x^2}+\frac{1}{h_y^2})\zeta^{m+1}_{j,k}-\frac{1}{h_x^2}\zeta^{m+1}_{j+1,k}-\frac{1}{h_x^2}\zeta^{m+1}_{j-1,k}-\frac{1}{h_y^2}\zeta^{m+1}_{j,k+1}-\frac{1}{h_y^2}\zeta^{m+1}_{j,k-1}]. \quad (20)$$

In order to solve the Poisson equation, the boundary condition for ψ is constructed from Eq. (15) in the following way:

$$\psi^{m+1}_{j,k}=\frac{H^2_{j,k}}{3T}[\frac{1}{h_x}(u^{m+1}_{j+1,k}-u^{m+1}_{j,k}-u^m_{j+1,k}+u^m_{j,k})+\frac{1}{h_y}(v^{m+1}_{j,k}-v^{m+1}_{j,k-1}-v^m_{j,k}+v^m_{j,k-1})]. \quad (21)$$

Description FNS-VOF Model

The FNS-VOF approach is used in this study to visualize differences and validate NLSW and NLB numerical models. The FNS equations include the vertical component of velocity/acceleration. The FNS-VOF approach solves a transient two-dimensional incompressible fluid flow with free surface. The finite difference solutions of the incompressible FNS equations are obtained on a rectilinear mesh.
Equation of continuity for incompressible fluid

$$\nabla \cdot \mathbf{u} = 0 \tag{22}$$

and the momentum equation

$$\frac{\partial \mathbf{u}}{\partial t} + (\mathbf{u} \cdot \nabla)\mathbf{u} = -\frac{1}{\rho}\nabla p + \nu \nabla^2 \mathbf{u} + \mathbf{g}, \tag{23}$$

are solved in a rectangular system of coordinates. Where $\mathbf{u}(x, y, t)$ is the velocity vector, ρ is the fluid density, p is the pressure, ν is the kinematic viscosity, $\mathbf{g}$ is the gravitational acceleration and t is the time. Solution of the equations is constructed using the two-step method, Chorin (1968); Harlow and Welch (1965). The time discretization of the momentum equation is given by

$$\frac{\mathbf{u}^{m+1} - \mathbf{u}^m}{T} = -(\mathbf{u} \cdot \nabla)\mathbf{u}^m - \frac{1}{\rho^m}\nabla p^{m+1} + \nu \nabla^2 \mathbf{u}^m + \mathbf{g} \tag{24}$$

and it is broken up into two steps as follows:

$$\frac{\tilde{\mathbf{u}} - \mathbf{u}^m}{T} = -(\mathbf{u} \cdot \nabla)\mathbf{u}^m + \nu \nabla^2 \mathbf{u}^m + \mathbf{g} \tag{25}$$

$$\frac{\mathbf{u}^{m+1} - \tilde{\mathbf{u}}}{T} = -\frac{1}{\rho^m}\nabla p^{m+1}. \tag{26}$$

Eq. (26) and the continuity equation (Eq. 22) can be combined into a single Poisson equation for the solution of the pressure as

$$\nabla \cdot [\frac{1}{\rho^m}\nabla p^{m+1}] = \frac{\nabla \cdot \tilde{\mathbf{u}}}{T}. \tag{27}$$

The free surface of the fluid is described by the discrete VOF function, introduced by Nichols and Hirt (1975) and Nichols *et al.* (1980). The Fluid is advected as a Lagrangian invariant, propagating according to

$$\frac{dF}{dt} = \frac{\partial F}{\partial t} + (\mathbf{u} \cdot \nabla)F = 0. \tag{28}$$

The scalar field $F(\vec{x}, t)$ is defined as:

$$F(\vec{x}, t) = \begin{cases} 1 & \text{in the fluid,} \\ 0 < F < 1 & \text{at the free surface,} \\ 0 & \text{in the void.} \end{cases}$$

OBSERVATIONS AND DISCUSSIONS

First, above numerical models are applied to a simplified case for the IOT (one-dimensional channel case) along transect A-A depicted in Fig. 2. This numerical experiment is intended to visualize dispersive effects using FNS-VOF model and test the NLSW (nondispersive) and NLB (dispersive) approaches. Transect A-A extends from 95.48^{o}E, 4.93^{o}N to 81.13^{o}E, 1.8^{o}S with total length of : 1745 Km. At both sides, the channel is bounded by walls, so the lateral interaction of waves is restricted, therefore, neither the wave is radiated from the channel nor outside signal is propagated into

channel. Model parameters and CPU time for the numerical computation are given in Table 1. The chosen time step ensures that water particles travel the computational cell in at least three time steps. In all models, several spatial resolutions have been applied to verify numerical convergence.

Model	δx	δz	δt	Num. of cells	CPU time
NLSW (Trans. A-A)	100 m	——	0.2 s	157059	30 min
NLB "	100 m	——	0.2 s	157059	5 h
FNS-VOF "	(5 – 875) m	(0.2 – 40) m	(0.08 – 0.8) s	800000	72 h

Table 1. Parameters for numerical computations along transect A-A (channel case)

Fig. 3 shows a series of free surface snapshots of the first 2 h of the IOT propagation based on the initial condition given by Kowalik *et al.* (2005). General features of the wave evolution agreed very well in all approaches. However, some differences in reproducing the dispersion phenomena become more noticeable as time advances. For instance, at time ≥ 40 min, the wave dispersion is evident according to NLB and FNS-VOF results. A train of waves which comprises multiple amplitudes and frequency components is formed immediately behind the leading wave. Major wave features are well reproduced by the NLSW method with exception of the train of waves. The leading NLSW wave is taller and shifted forward in space in relation to the dispersive solutions. The nondispersive NLSW approach overpredicts by ~28% the wave height at time 2 h 5 min. A slight advance in time (2 min 15 s) of the NLSW leading wave crest is observed as well. However, the wave front tip of the NLSW leading wave matches very well to its counterpart. This reaffirms the use of NLSW as an accurate approximation for determining the tsunami arrival time.

NLB and FNS-VOF model results agreed better in reproducing the detailed features such as the spatial and temporal distributions of the leading dispersive wave. However the NLB train which follows the leading wave is shifted forward in time with respect to FNS-VOF train. The shift increases in time as the wave diminishes in amplitude and length as shown in the zoomed window of Fig. 3. Values of $kh = (2\pi/L)h$ for the first, second and third waves at time 2 h 5 min according to FNS-VOF results are 0.17, 0.46 and 0.56 respectively ($h = 4810$ m). Their respective wavelengths are L =[179, 89 and 65]km, measured from trough to trough. Although the second and third waves fall into category of intermediate water wave regime ($0.31 < kh < 3.14$) the approximation of the dispersive term in the NLB model gives accurate estimate of the wave speed because the value of $kh < 1$ (Wei and Kirby, 1995). In comparison to the linear dispersion relation, the error is less than 1%. Although the second, third and subsequent NLB model waves shift slightly forward in relation to the FNS-VOF results, the NLB model predicts well the wave height, wave length and number of waves in the wave train.

The study is extended to visualize the wave dispersion effects in two-dimensions in the Bay of Bengal basin. Now, the computational domain is bounded by the window 78^{o}E, 1^{o}N to 100^{o}E, 14^{o}N. In this experiment, only NLB and NLSW models are used. At all open boundaries wave radiation condition is applied. Model parameters and CPU

time for the numerical computation are given in Table 2.

Model	δx	δy	δt	Num. of cells	CPU time
NLSW	1 min	1 min	3 s	1249600	16.0 min
NLB	1 min	1 min	3 s	1249600	1.5 h

Table 2. Parameters for the numerical computation for the two-dimensional case (Bay of Bengal)

Fig. 4 shows wave patterns at time 1 h 40 min using NLSW and NLB methods. Due to the dispersion effects the NLB model shows a series of wave behind the leading wave, therefore, wave patterns are significantly different from that of NLSW model. From the NLB model result, it is seen that length of the wave train in western region is longer than in the eastern region (close to Thailand and Indonesia). As Eqs. (13) and (14) suggest the magnitude of the dispersive term is proportional to the square of water depth, therefore, the dispersion effect in the western region ($H = 4\text{-}5$ km) is stronger than that in the eastern region (which is only of several hundred meters deep). Additionally the dispersion effect in the western region is enhanced through the longer distance of propagation.

Fig. 5 shows temporal variation of the free surface obtained by NLSW and NLB models at locations of numerical gauges given in Fig. 2. Again, over all agreement between nondispersive and dispersive models is very good. The same dispersive pattern is observed as in the channel along transect A-A. At gauge 1, agreement between dispersive and nondispersive solutions is excellent due to the proximity of the gauge to the tsunami source, as dispersive waves do not have time to develop. On the other hand, the sea level recorded at gauges 2 and 3, features dispersive waves since the gauges are located farther away from the tsunami source. The leading wave height is overpredicted again by the NLSW solution by 22% at gauge 2 and by 14% at gauge 3. A shift in time between leading wave crests is noticed as well; 50 s at gauge 2 and 1 min 5 s at gauge 3. Note the good agreement of the NLSW and NLB leading wave front tip in all gauge records.

The last experiment is intended to visualize the implication of dispersive effects on the runup. Two transects, B-B and C-C, have been chosen as indicated Fig. 2. One transect is in the Northwest of Sumatra (close to Banda Aceh); this location was struck by a "near-field" tsunami. In contrast, the other one across the Bay of Bengal, Sri Lanka (close to Yala), experienced a "far-field" tsunami. The rapid arrival of the tsunami to the near-field location in approximately 15 to 20 min, is juxtaposed with a longer arrival time of around 2 h to the far-field location. The numerical domains extend from 95.09^{o}E, 5.47^{o}N to 95.3^{o}E, 5.47^{o}N (transect B-B), and from 81.78^{o}E, 6.35^{o}N to 81.45^{o}E, 6.35^{o}N (transect C-C). At the offshore end of the channels the temporal variations of the free surface from the two-dimensional computation are established as boundary forcing. This experiment is intended to investigate the implication of dispersive effects on the runup, therefore, the two-dimensional contribution is avoided by constructing channels to visualize the approach of the wave train to the shoreline. Unfortunately, the 1 min

resolution is too coarse to represent a runup. For the purpose of this experiment a fine grid size was constructed in the models, using linear interpolation, to fill the gaps in the available bathymetry. A 10 m spatial resolution is applied in both experiments. Model parameters and CPU time for numerical computations are given in Table 3.

Model	δx	δy	δt	Num. of cells	CPU time
NLSW (Trans.B-B)	10 m	--	0.2 s	22680	4 min
NLB "	10 m	--	0.2 s	22680	30 min
NLSW (Trans.C-C)	10 m	--	0.2 s	34020	5 min
NLB "	10 m	--	0.2 s	34020	40 min

Table 3. Parameters for the numerical computation for one-dimensional cases: Banda Aceh, Sumatra (transect B-B) and Yala, Sri Lanka (transect C-C).

Figs. 6, 7 and 8 show tsunami propagation and runup in the coastal regions obtained by the NLSW and NLB models. In both experiments the computed maximum runup heights calculated by both methods are approximately 10 m. These results agree with the observed maximum runup in Yala (http://www.drs.dpri.kyoto-u.ac.jp/sumatra/srilanka-ut/SriLankaU_Teng.html), but underestimate the observed one in Banda Aceh (http://www.eri.u-tokyo.ac.jp/namegaya/sumatera/surveylog/eindex.htm).

Fig. 6 shows snapshots of the runup at Banda Aceh at extreme stages. Regardless of the models, free surface profiles, timing and runup heights match very well. Fig. 7 shows tsunami propagation on the continental shelf at Yala, Sri Lanka. As the wave approaches to the shoreline the dispersive effects are enhanced as revealed through the NLB solution. Subsequent snapshots at the shoreline (Fig. 8) show that the runup heights of the leading wave are almost the same in both models. However, Fig. 8c (3 h 7 min) shows that a higher runup is obtained by the NLB solution (37 min after leading wave runup), which is about 60% higher than the runup obtained by the NLSW model. Thus, dispersion consideration in numerical models is necessary for accurate prediction, since dispersion can produce significant differences in coastal runup. Dispersive waves interacting with the natural frequencies of the continental shelf, bay or harbor tend more often to generate resonance as compared to the long waves.

CONCLUSIONS

We have compared three approaches to compute tsunami, i.e., the nonlinear shallow water (NLSW nondispersive), the nonlinear Boussinesq (NLB) and the full Navier-Stokes aided by the volume of fluid method (FNS-VOF). The FNS-VOF method gives a frame of reference to validate the NLB and NLSW solutions. Since this approach introduces the vertical fluid velocity/acceleration and column-wise discretization, more accurate results are expected. However this method still requires higher computational resources, often not available for practical tsunami computations.

Comparison of the three different methods shows that for practical purpose the NLSW model results are quite reliable, since this model gives consistent results with its counterparts. The NLSW approach is very attractive nowadays for tsunami calculation because this method have very low computational cost and maximum wave height and

runup are often overpredicted, thus increasing safety factor. The NLSW results are useful for preliminary hazard assessment, where a simple and quick estimation of maximum wave height, maximum run-up and locations of maxima are required. Determination of the wave front tip location for the IOT is excellent. This reaffirms its use as an accurate method for determining the tsunami arrival time.

Qualitatively and quantitatively the wave fronts reproduced by the NLB and FNS-VOF solutions share many common features. For the longer integration time the similarity holds only for the main maximum, because the phase differences between secondary maxima increase with travel time (Fig. 3). Tsunami patterns away from the main front including runup have been reproduced by all three methods quite well and the sea level differences are quite small. The dispersion consideration in the numerical models is necessary for accurate prediction since it can produce significant differences in coastal runup when the wave front depicted in Fig. 7 will impinge on the coast creating complicated patterns of oscillations as compared to the NLSW solution given in Fig. 8. Such oscillations arriving to the continental shelf, bays or harbors may enhance the tsunami oscillations through the resonance. As Ortiz *et al.* (2001) pointed out the dispersion mechanism is not clearly established from the coastal observations, because such data are strongly influenced by the local bathymetry. Does IOT provide such validation? The general comparisons between data and NLSW model results given for IOT by Kowalik *et al.* (2005), Lay *et al.* (2005) and Hirata *et al.* (2005) are quite good even though these are nondispersive models. Preliminary results from the dispersive model of IOT presented by Watts *et al.* (2005) still require comparison with the NLSW. The computations in the nearshore regions will shed farther information on the dispersive versus nondispersive processes in IOT, however to undertake this direction fine resolution bathymetry is needed.

REFERENCES

Chorin, A. J. 1968. Numerical solution of the Navier-Stokes equations. *Math. Comp.* 22:745-762.

Dunbar, D., P. Leblond and T. S. Murty. 1991. Evaluation of tsunami amplitudes for the Pacific Coast of Canada. *Prog Oceanog.* 26: 115-177.

Fujima, K. 2001. Long wave propagation on large roughness. *ITS Proceedings, Sec. 7*, 7(22):891-895.

Goto, C. and N. Shuto. 1983. Numerical simulation of tsunami propagations and run-up. In *Tsunami-Their Science and Engineering*, edited by K. Iida and T. Iwasaki, pp 439-451. Tokyo: Terra Scientific Publ. Comp.

Harlow, F. H. and J. E. Welch. 1965. Numerical Calculation of time-dependent viscous incompressible flow of fluid with a free surface. *The Physics of Fluids* 8:2182–2189.

Heinrich, P., F. Schindele and S. Guiborg. 1998. Modeling of the February 1996 Peruvian tsunami. *Geophys. Res. Lett.* 25(14), 2687-2690.

Hirata, K. , K. Satake, Y. Tanioka, T. Kuragano, Y. Hasegawa, Y. Hayashi, and N. Hamada. 2005. The Indian Ocean Tsunami: Tsunami Source Model From Satellite Altimetry. *Proceedings of the International Tsunami Symposium*, edited by G.A. Papadopoulos and K. Satake, Chania Greece, pp 72-76.

Imamura, F., N. Shuto, and G. Goto. 1988. Numerical simulation of the transoceanic propagation of tsunamis. *th Congress Asian and Pacific Regional Division,*

International Association for Hydraulic Research, Kyoto Japan 6: 265-272.

Imamura, F. and N. Shuto. 1989. Tsunami propagation simulation by use of numerical dispersion. *International Symposium on Computational Fluid Dynamics* pp.390-395.

Imamura, F., N. Shuto and C. Goto. 1990. Study on numerical simulation of the transoceanic propagation of tsunamis. Part 2, Characteristics of tsunami propagation over the Pcific Ocean. *Zisin (J, Seismol. Soc. Japan)*, 43,389-402.

Kowalik, Z. and T. S. Murty. 1993a. *Numerical Modeling of Ocean Dynamics*, Singapore: World Scientific.

Kowalik, Z. and T. S. Murty. 1993b. Numerical Simulation of Two-Dimensional Tsunami Runup, *Marine Geodesy*, 16:87-100.

Kowalik, Z., W. Knight, , T. Logan, and P. Whitmore. 2005. Numerical Modeling of the Global Tsunami: Indonesia Tsunami of 26 December 2004. *Science of Tsunami Hazards* 23 (1): 40-56.

Kulikov, E. 2005. Dispersion of the Sumatra Tsunami Waves in the Indian Ocean detected by satellite altimetry. http://www-sci.pac.dfo-mpo.gc.ca/osap/projects/tsunami/documents/195610_0_merged_1107633516.pdf

Lay, T., H. Kanamori, C. J. Ammon, M. Nettles, S. N. Ward, R. C. Aster, S. L. Beck, S. L. Bilek, M. R. Brudzinski, R. Butler, H. R. DeShon, G. Ekstrom, K. Satake, S. Sipkin. 2005. The Great Sumatra-Andaman Earthquake of 26 December 2004. *Science*, 308: 1127-1139.

Liu P.L.-F., Y. B. Cho, S. B. Yoon and S. N. Seo. 1995. Numerical simulation of the 1960 Chilean tsunami propagation and inundation at Hilo, Hawaii. In *Tsunami Progress in Prediction, Disaster Prevention and Warning*, edited by Y. Tsuchiya and N. Shuto. Netherlands: Kluwer Academic Publisher.

Madsen, P. A., and H. A. Schaffer. 1999. A review of Boussinesq-type equations for surface gravity waves. In *Advances in Coastal and Ocean Engineering*, edited by P. L.-F. Liu, vol. 5, pp 1-94. Singapore: World Scientific.

Mader, C. L. 2004. *Numerical Modeling of Water Waves*, Boca Raton: CRC Press.

Nichols, B. D. and C. W. Hirt. 1975. Method for Calculating Multi-Dimensional, Transient Free Surface Flow Past Bodies. *Proc. of the 1st Int. Conf. Num. Ship Hydrodynamics*, Gaithersburg, Maryland.

Nichols, B. D., C. W. Hirt and R. S. Hotchkiss. 1980. SOLA-VOF: A Solution Algorithm for Transient Fluid Flow with multiple Free Boundaries. *LA-8355, Los Alamos National Laboratory*.

Okada, Y. 1985. Surface deformation due to shear and tensile faults in a half-space. *Bulletin of the Seismological Society of America* 75: 1135-1154.

Ortiz, M., E. Gómez-Reyes, H.S. Vélez-Muñoz. 2001. A fast preliminary estimation model for transoceanic tsunami propagation. *ITS 2000 Proceedings* 723-739.

Sato, S. 1996. Numerical simulation of 1993 southwest Hokkaido earthquake tsunami around Okushiri Island. *J. Waterway, Port, Coastal and Ocean Eng.* 122 (5): 209-215.

Shigihara, Y. 2004. A study on application of non-linear dispersive wave theory to the numerical simulation of tsunami. PhD Thesis, Dept. of Engineering, Tohoku University (in Japanese).

Shigihara, Y., K. Fujima, M. Homma and K. Saito. 2005. Numerical methods of linear dispersive wave equation for the practical problems. *Asian and Pacific Coasts, 2005*,

Sept. 4-8, Jeju, Korea, paper pp 14.

Yoon, S. B. 2002. Propagation of distant tsunamis over slowly varying topography. *J. Geoph. Res.* 107 (c10, 4-1): 4-11.

Watts, P., Ioualalen, M., Grilli, S., Shi, F., and Kirby, J. T. 2005. Numerical simulation of the December 26, 2004 Indian Ocean tsunami using high-order Boussinesq model, *Fifth Int. Symp. WAVES 2005, July, 2005, Madrid Spain*, 10pp.

Wei, G. and Kirby, J. T., 1995, A time-dependent numerical code for extended Boussinesq equations, *Journal of Waterway, Port, Coastal and Ocean Engineering*, **120**, 251-261

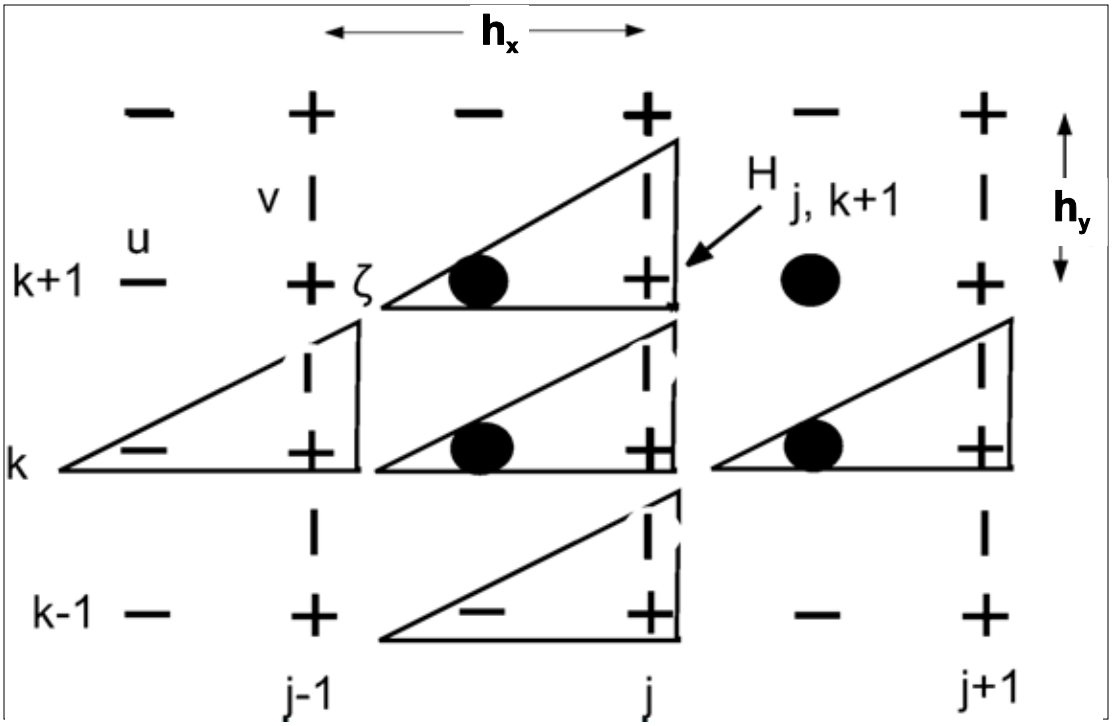

Figure 1. Spatial grid distribution .

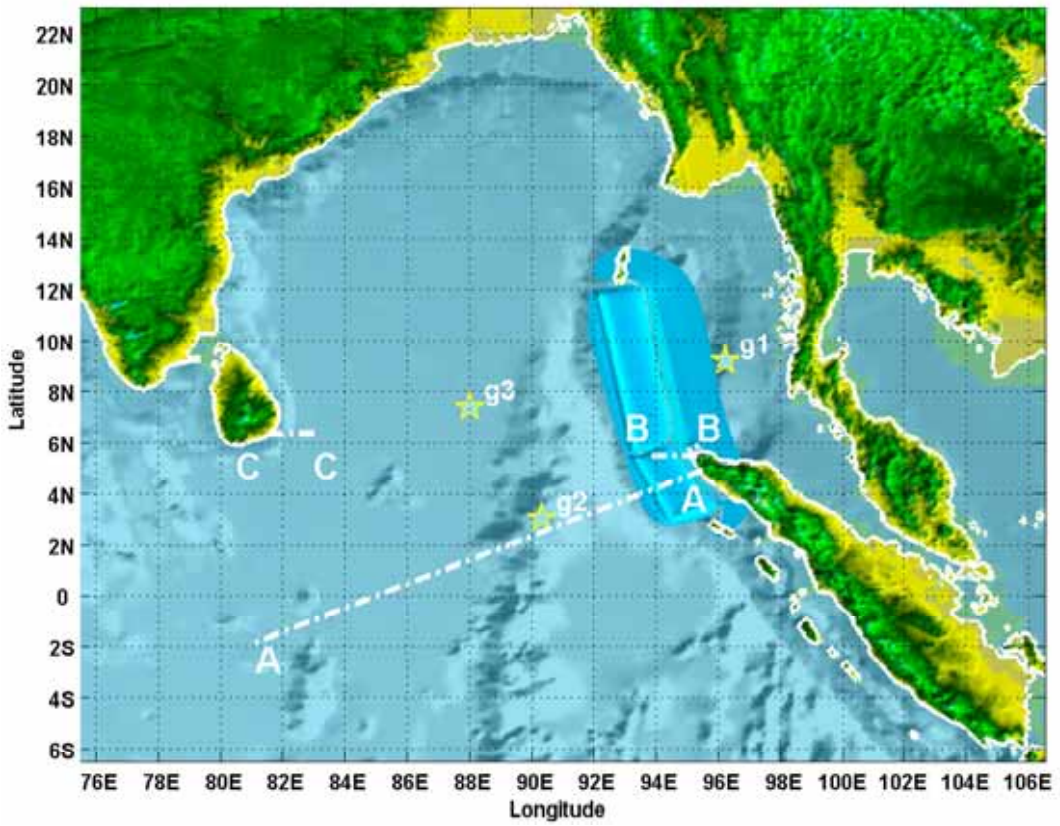

Figure 2. Indian Ocean bathymetry, initial free surface deformation and location of numerical gauges and transects

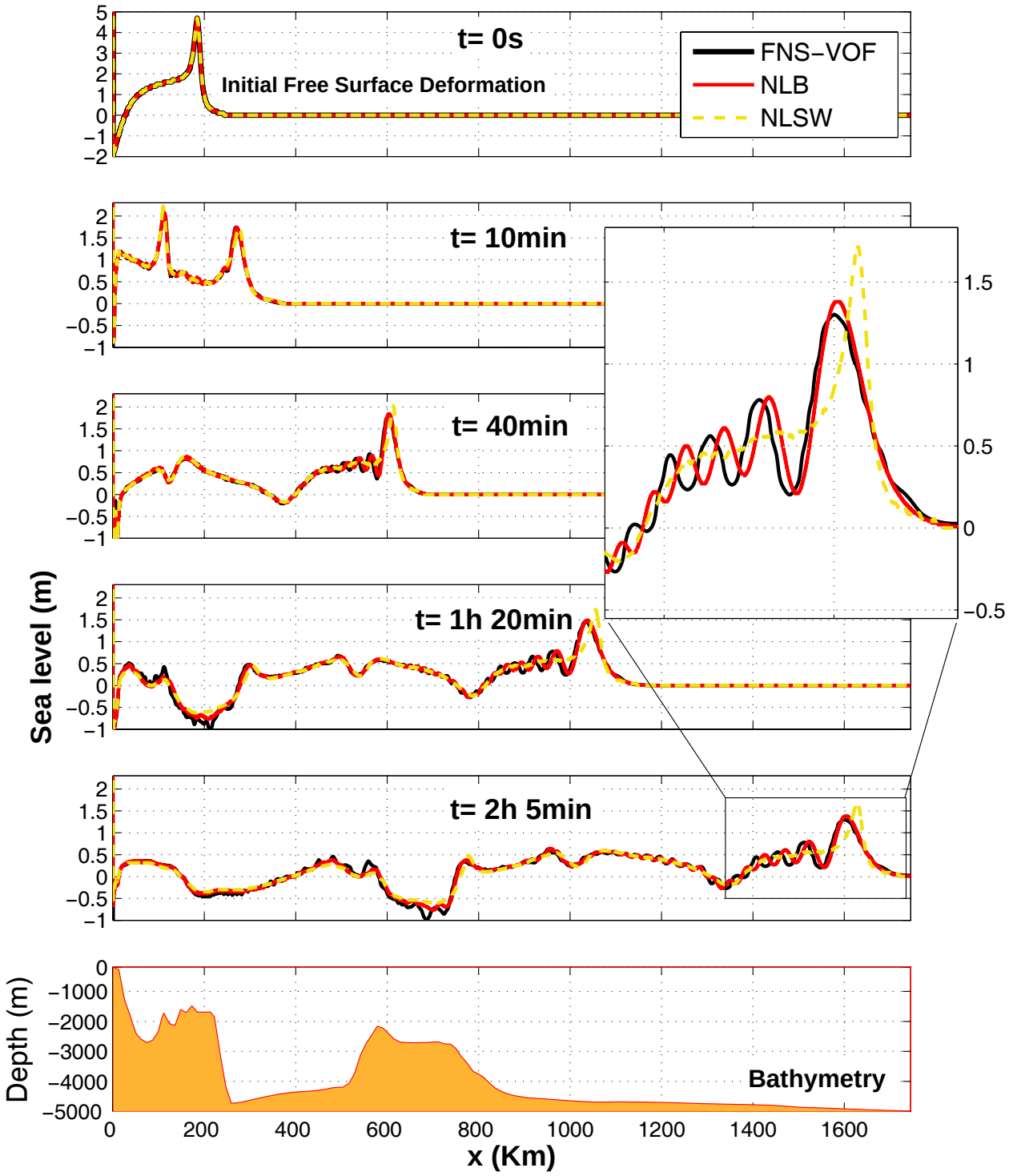

Figure 3. Tsunami propagation along transect A-A computed by three different methods

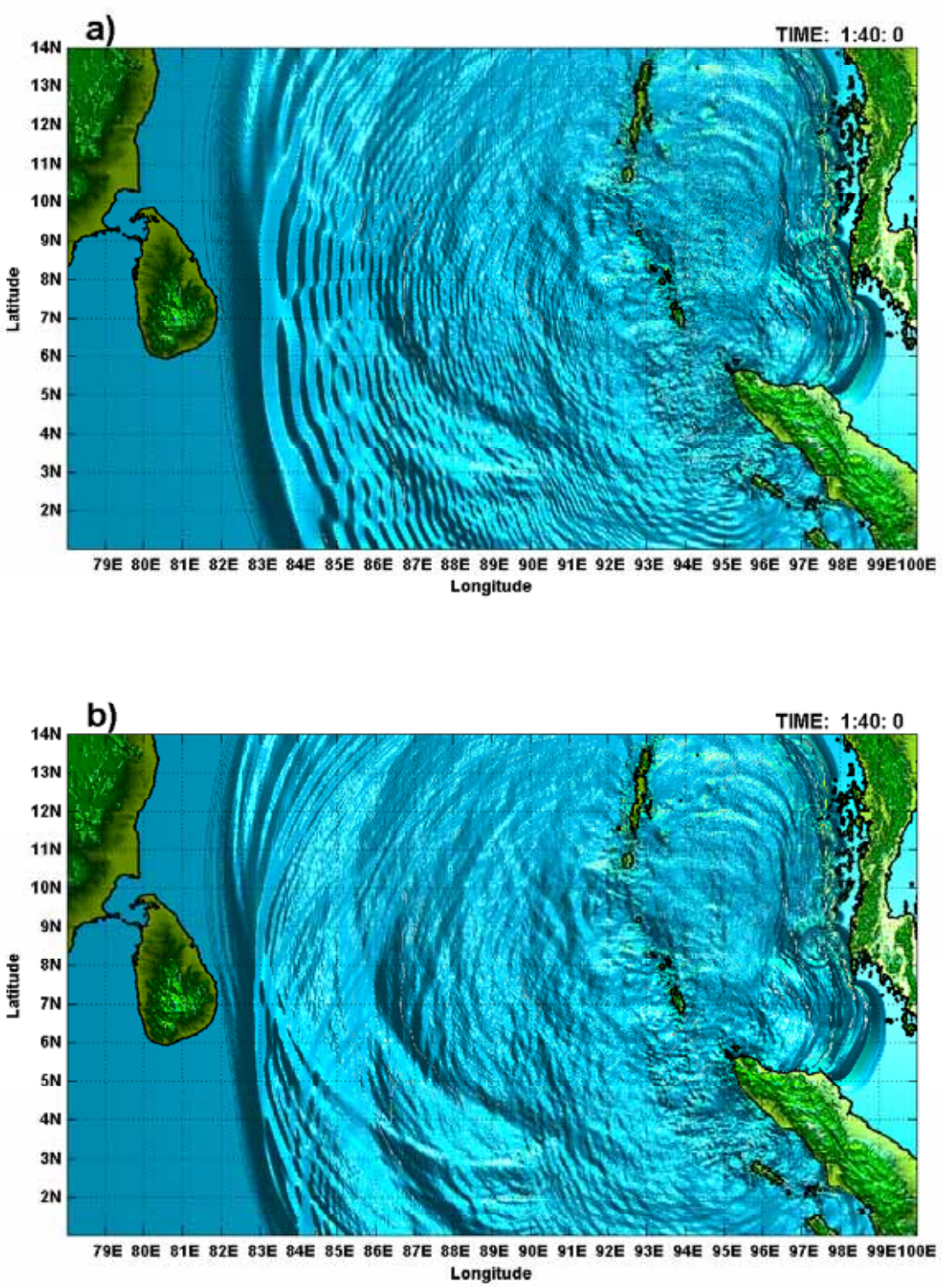

Figure 4. Comparison of water surface computed at 1h 40min from the onset of the earthquake: a) NLB model results, and b) NLSW model results

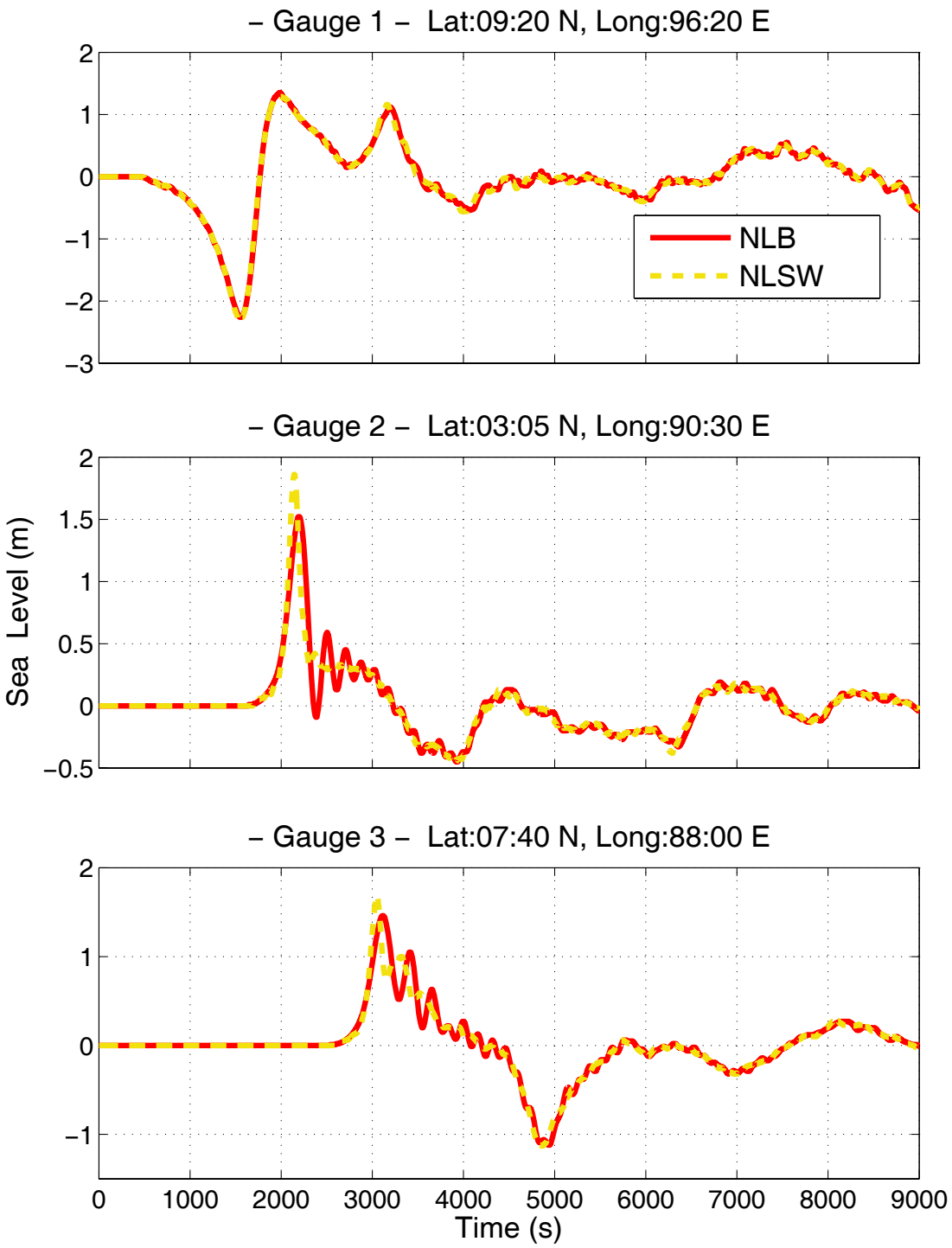

Figure 5. Comparison of water level at different locations (given in Fig. 2) obtained by NLB and NLSW models

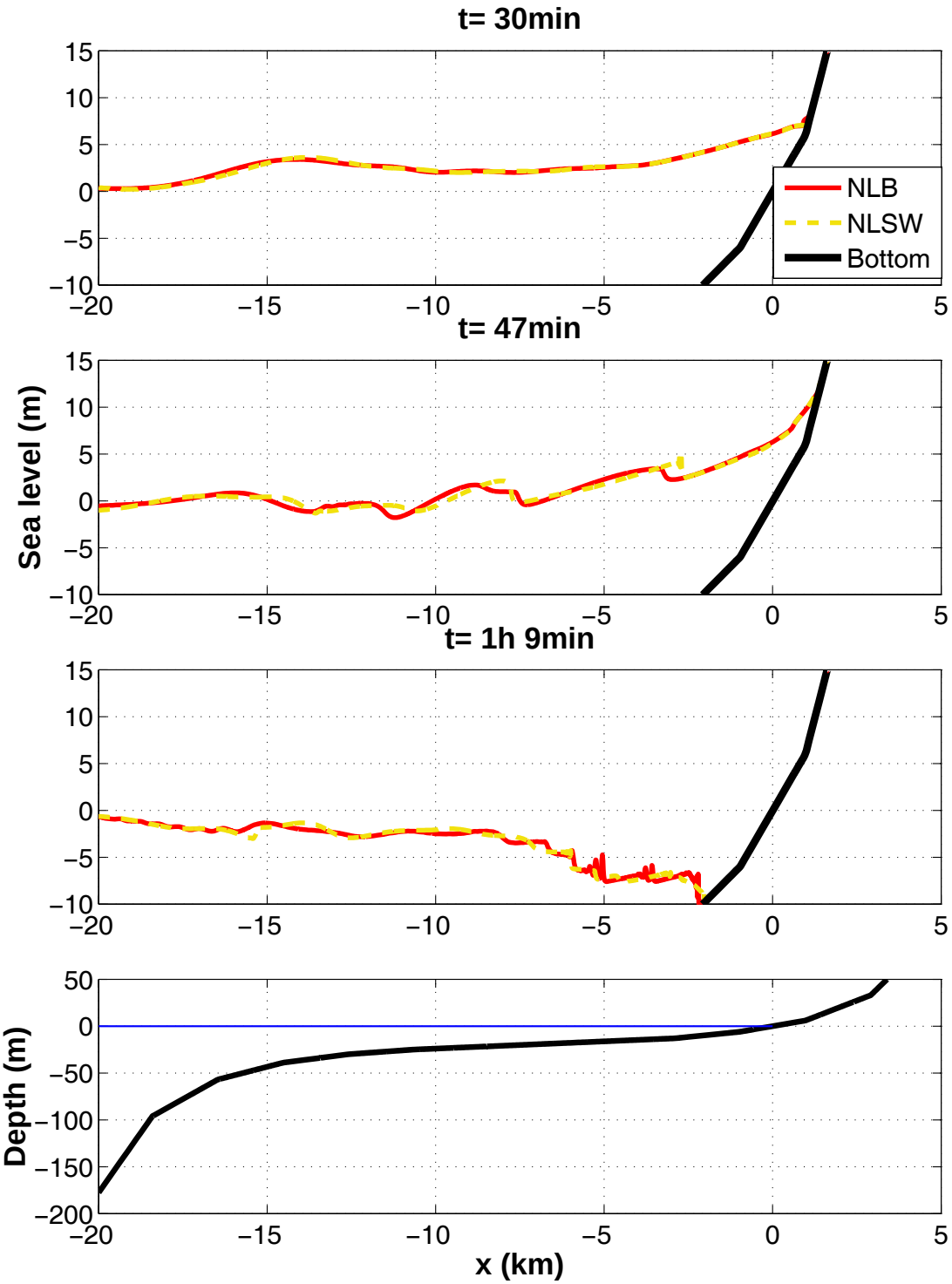

Figure 6. Comparison of tsunami runup/rundown at Banda Aceh, Sumatra (transect B-B), obtained by one-dimensional NLB and NLSW models.

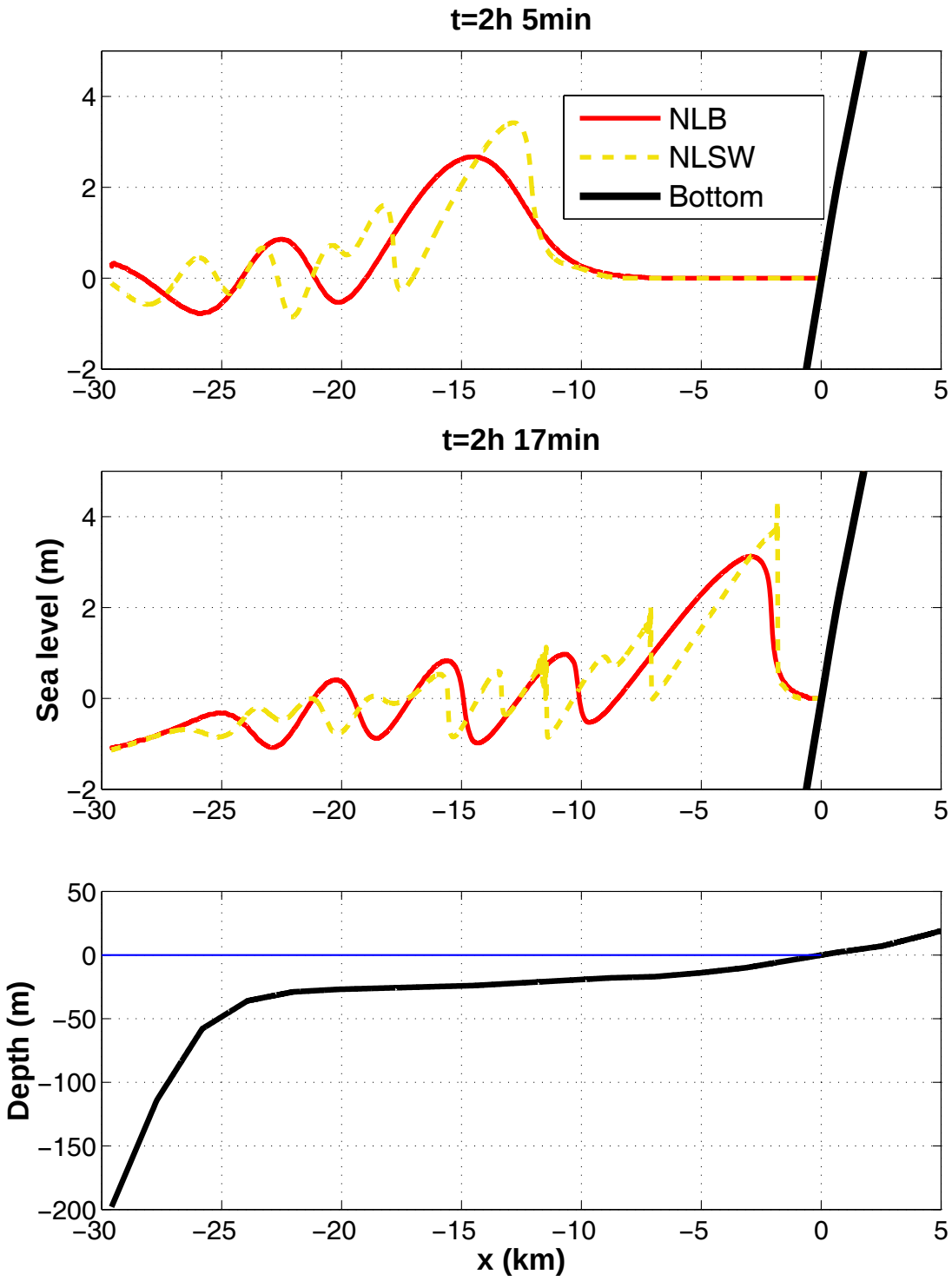

Figure 7. Comparison of tsunami propagation on the continental shelf at Yala, Sri Lanka (transect C-C), obtained by one-dimensional NLB and NLSW models.

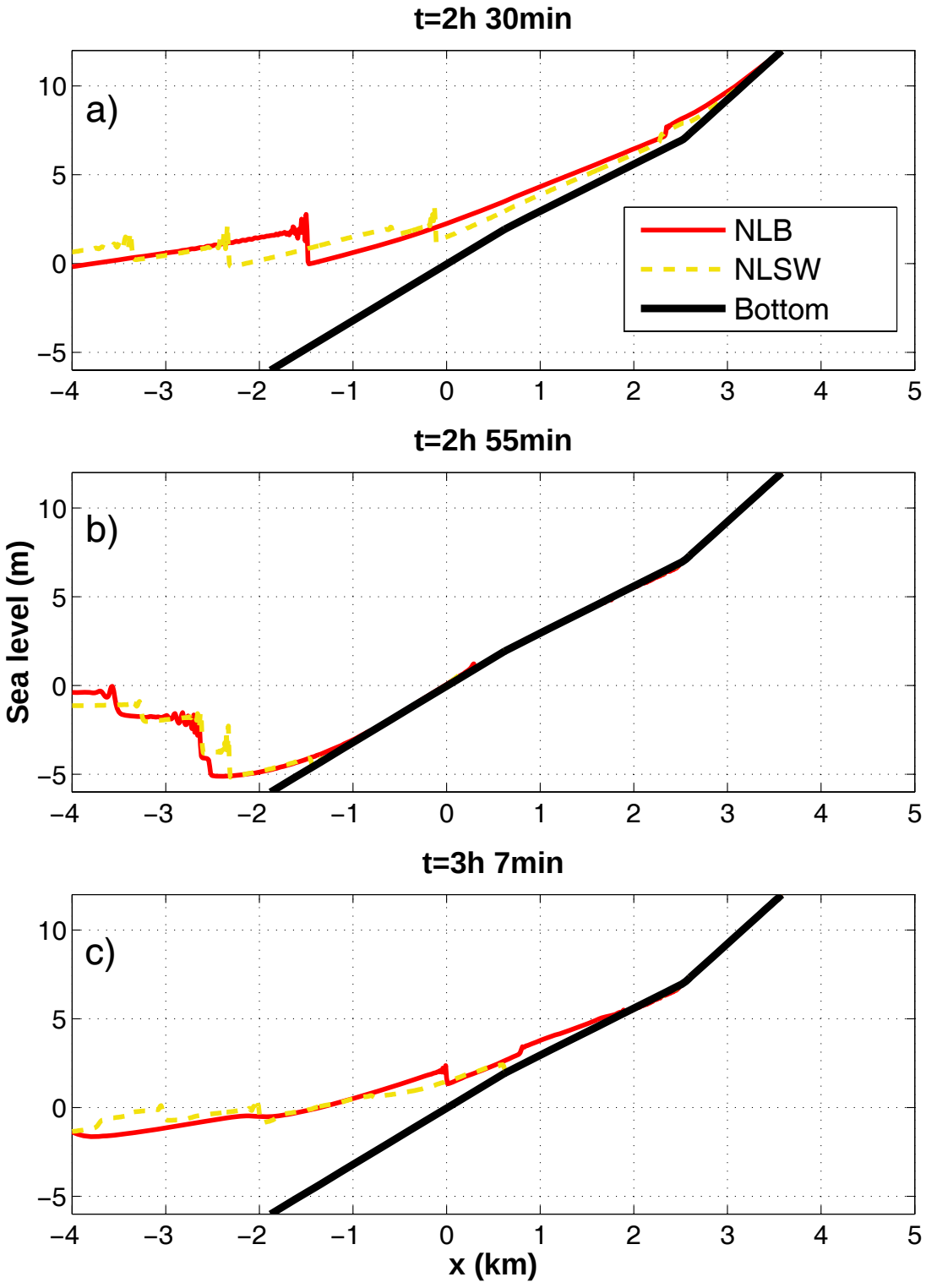

Figure 8. Comparison of tsunami runup/rundown at Yala, Sri Lanka (transect C-C), obtained by one-dimensional NLB and NLSW models.